

## A PANEL FREE-WAKE CODE WITH BOUNDARY LAYER METHOD FOR HELICOPTER SIMULATIONS

Philipp Kunze, [Philipp.Kunze@dlr.de](mailto:Philipp.Kunze@dlr.de), German Aerospace Center (DLR), Germany

### Abstract

UPM, DLR's unsteady panel and free-wake code for helicopter simulations, is being modernized and extended in order to provide a modern mid-fidelity tool suitable to support the industrial helicopter development process. Two major tasks in this process were the implementation of approximate boundary layer analysis methods and the calculation of unsteady pressures on arbitrary bodies. This paper shortly describes UPM and the newly implemented methods. Then, results of verification and validation calculations are presented, including isolated airfoil, wing, rotor and fuselage test cases. Finally, a complete helicopter configuration is simulated and compared to experimental wind tunnel results of the GOAHEAD campaign. The results show that the approximate boundary layer methods are able to identify flow separation regions and provide reasonable friction force estimates for a wide range of applications. Nevertheless, the limits of the methods become apparent in cases where viscous effects lead to strong nonlinear behavior. The complete helicopter simulation also shows a good agreement with experimental data in general. But here, too, individual flow regions reveal the limits of the underlying theory. If these limits are kept in mind, UPM can be a valuable tool and support the helicopter development process in many regards.

## 1 INTRODUCTION

DLR's unsteady 3D panel and free-wake code UPM [1] is being enhanced in order to supplement the industrial helicopter development process by filling the gap between well-established low-fidelity and high-fidelity methods for the prediction of aerodynamic interactions. An important field of application is the identification of potentially critical flight states in the flight envelope of a helicopter, which can then be selectively investigated using higher-fidelity simulations. Flow separation and other viscous effects account for many critical flight states. Thus, there is a demand for viscous analysis features within UPM which enable the identification of flow separation areas and return an estimate of frictional forces. This demand was addressed as a major activity in the project CHARME. In a first step, various possible analysis methods were evaluated regarding several rating criteria and requirements. Rapidity, robustness, and user friendliness were taken as key requirements. As a result of this evaluation process, two approximate boundary layer analysis approaches were selected and implemented. The first one is used for lifting surfaces and bases on stripwise analysis along spanwise/radial segments using integral boundary layer methods. A similar approach for unstructured non-lifting bodies was classified as too complex and error-prone for the intended applications regarding unsteady flow and strong component interactions. Thus, a simplified boundary layer analysis method based on local flow properties and flat-plate analogy was implemented for non-lifting bodies. It was combined with simple flow separation criteria in order to enable the prediction of separated flow regions on arbitrary bodies.

The newly implemented methods for approximate boundary layer analysis were tested and compared for several test cases, including isolated airfoils, wings, rotors and fuselages. Furthermore, an unsteady surface pressure calculation method for unstructured bodies was implemented and a validation simulation of a complete helicopter configuration was performed.

## 2 COMPUTATIONAL METHOD

### 2.1 Unsteady Panel and Free-Wake Method

UPM [1] is a research code originally intended for aero-acoustic simulations of rotorcraft, especially regarding BVI-noise (Figure 1). In this context it was validated and applied extensively, e.g. for an isolated rotor [2], a complete helicopter [1], propeller-wing and engine exhaust interaction [3], and arbitrary complex configurations [4]. In parallel, the field of application was constantly extended, e.g. for rotor performance optimization [5] and evaluation of aerodynamic interactions regarding rotor-rotor and rotor-fuselage [6] or obstacle-rotor [7] cases. Rinker et al. [8] utilized UPM for the assessment of rotor-stabilizer interactions and demonstrated its suitability for the prediction of unsteady tail loads induced by the rotor.

UPM uses a velocity based potential flow formulation with Neumann boundary conditions. The flow around arbitrary non-lifting bodies is simulated analogous to the classical Hess-Smith panel code [9]. Body surfaces are discretized using quadrilateral and/or triangular panels with constant sink/source distribution as singularity elements. Lifting surfaces are discretized using structured panel surfaces, consisting only of quadrilateral constant sink/source panels. In order to

account for lift generation, the source panels are superposed by a vortex lattice on the mean surface of the lifting bodies (Figure 2). At the trailing edge, a full-span free wake vortex sheet consisting of constant strength vortex rings is emitted and transported through the flow-field in a force-free way, simulating the unsteady wake rollup. A second-order Adams-Bashforth method is used for temporal integration. The velocities induced by the wake can optionally be evaluated using a tip-vortex rollup model, as described in [10] and [11]. Besides the classical Kutta condition, an iterative pressure Kutta condition as described in [12] is available. It enforces equal pressure at the trailing edge panels of the upper and lower sides and thus takes unsteady pressure terms into account when solving the flow around lifting bodies.

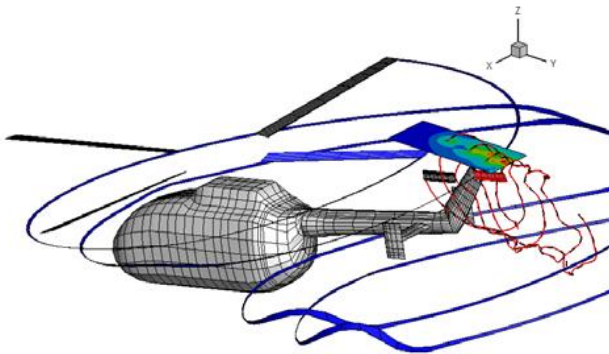


Figure 1: Exemplary UPM simulation of a complete helicopter in descent flight [1]

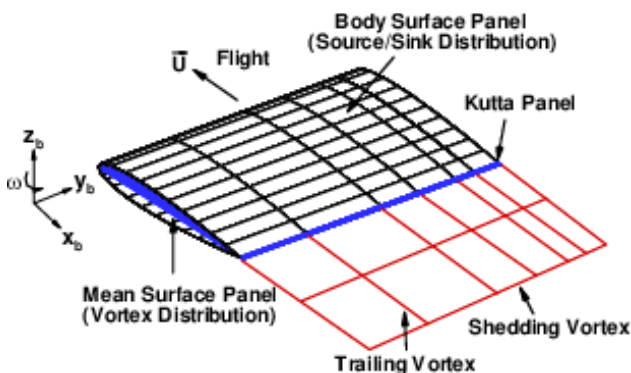


Figure 2: UPM lifting surface model [1]

## 2.2 Unsteady Surface Pressure Calculation

Unsteady pressures are calculated using the unsteady Bernoulli equation:

$$c_p = 1 - \frac{U^2}{U_\infty^2} - \frac{2}{U_\infty^2} \frac{\partial \phi}{\partial t}$$

UPM uses a velocity-based formulation, therefore the second so-called “quasi-steady” term can be calculated easily. But neither the velocity potential  $\phi$  nor its temporal derivative are readily available and thus must be calculated before being able to evaluate the last so-called “unsteady” term. The contribution of the sink/source panels to the velocity potential is calculated directly using influence coefficients. For the

contribution of the bound and free-wake vortices two approaches are available:

1. The velocity potential on structured lifting surfaces is evaluated by sectional integration of induced velocities from leading edge to trailing edge. Its temporal derivative is calculated using backward finite differences.
2. On arbitrary unstructured surfaces the contribution of a vortex element to the  $\partial \phi / \partial t$  term is calculated “by negative the dot product of the convection velocity of the vortex element relative to a point on the surface and the velocity the element induces at that point”, according to [13].

## 2.3 Approximate Boundary Layer Analysis

The implemented approximate boundary layer analysis methods are outlined in this section. For a more detailed description the reader is referred to [14].

### 2.3.1 Sectional Boundary Layer Analysis

For lifting surfaces (i.e. rotors, stabilizers, wings), stripwise boundary layer analysis using integral methods is employed in order to calculate the chordwise and spanwise boundary layer properties. For each segment, the analysis starts with the detection of the stagnation point. As soon as the stagnation point is located, the segment is divided into a lower and an upper strip, each starting at the stagnation point and ending at the trailing edge. Then, input data required for the integral boundary layer analysis is extracted for each point along both strips. It consists of point coordinates and velocity components in chordwise and spanwise direction. Furthermore, the local onflow conditions of the segment (i.e. local reference velocity and viscosity) are gathered. Using this information, an integral boundary layer analysis is performed for both strips, each consisting of the following steps:

#### 1. Laminar Analysis

If the analysis mode was not set to fully turbulent, the boundary layer analysis starts by employing one of the implemented integral methods for laminar flow. A method according to Eppler [15], [16], [17] is used per default and for all simulations presented in this paper. At the end of each integration step the active boundary layer transition criteria are checked. The integration stops if transition is predicted or a condition for laminar flow separation is true or the end of the streamline is reached.

#### 2. Laminar-Turbulent Transition

The following transition mechanisms are currently implemented and may trigger the switch from laminar to turbulent analysis:

1. *Forced transition*: Boundary layer trips can be simulated by prescribing the location  $x_{tr}/c$

at which the calculation is continued using a turbulent method.

2. *Turbulent reattachment after laminar flow separation*: If laminar separation is predicted by the laminar analysis method, a condition given in [18] is used to determine whether the flow stays separated or reattaches as turbulent flow. If turbulent reattachment is predicted, it is assumed to occur immediately after laminar separation.
3. *Transition due to Tollmien-Schlichting (TS) instabilities*: Several empirical criteria for determining TS transition were implemented. A criterion based on an  $e^n$  envelope approximation by Arnal given in [19] is used per default.

### 3. Turbulent Analysis

If any of the mechanisms triggers transition, the boundary layer analysis is continued using a turbulent integral method. A turbulent integral method according to Eppler [15], [16], [17] is employed per default and in all simulations presented in this work. It stops if a condition for turbulent flow separation evaluates true or if the end of the streamline is reached. If separation is predicted, the boundary layer properties are assumed to be constant until the end of the streamline. Skin friction is set to zero in this region.

### 4. Mapping integral boundary layer properties back to the surface

The integral boundary layer properties determined along the strips in the previous steps are mapped back to the surface.

### 5. Calculation of friction loads

Finally, sectional and total forces and moments due to skin friction are calculated by surface integration of the local skin friction forces determined by the boundary layer analysis.

Laminar, transition, and turbulent methods can be selected by the user and combined arbitrarily. The presented approach does not model the mutual interaction of boundary layer displacement and potential flow by viscous-inviscid coupling. It is solely implemented as a postprocessing step without feeding the flow displacement effect back to the potential flow solver.

## 2.3.2 Simplified Analysis for Fuselages

A simplified turbulent analysis method for skin friction and flow separation region estimation for arbitrary non-lifting bodies was implemented. It is based on local flow properties and flat-plate analogy. The local skin friction on the body surface is assumed to correspond to the skin friction of a turbulent flat plate at equal streamline arc length and local potential flow velocity. Therefore, the determination of the local streamline arc length plays a central role in this method. In detail, the following steps are performed:

### 1. Local streamline arc length computation

An advancing front algorithm starting at stagnation panels and advancing based on a surface flux formulation over panel edges was developed to robustly calculate the approximate streamline arc length at each panel collocation point. It works on unstructured surface meshes consisting of triangular and/or quadrilateral panels.

### 2. Skin friction coefficient estimation

Using the local streamline arc length  $s$  and the local potential flow velocity  $U$  the local Reynolds number  $Re_s = \frac{U \cdot s}{\nu}$  is calculated and used to evaluate an approximate relation for the local skin friction coefficient  $c_f$  of the turbulent flat plate, as given by Schlichting [20]:

$$c_{f,loc} = [2 \cdot \log_{10}(Re_s) - 0.65]^{-2.3}, Re_s < 10^9$$

### 3. Separation region estimation

Two criteria for the prediction of areas of separated flow are available:

#### a) Angle criterion

The simple angle criterion is based on pre-design considerations and experimental results found in [21] and [22]. They suggest that flow separation occurs if the flow redirection angle exceeds a certain critical value. Therefore, the angle between the local panel normal vector  $\vec{n}$  and the global onflow direction  $\vec{U}_\infty$  is calculated for each panel as follows:

$$\rho_{loc} = \arccos\left(\frac{\vec{U}_\infty \cdot \vec{n}}{|\vec{U}_\infty| \cdot |\vec{n}|}\right) - 90^\circ$$

The global onflow direction is assumed to be the negative translational motion direction of the fuselage. Flow separation is predicted, if the following two conditions evaluate true:

1.  $\frac{\partial U}{\partial s} > 0$  (separation only occurs in regions of retarded flow)
2.  $|\rho_{loc}| > \rho_{sep}$  (separation threshold angle is exceeded)

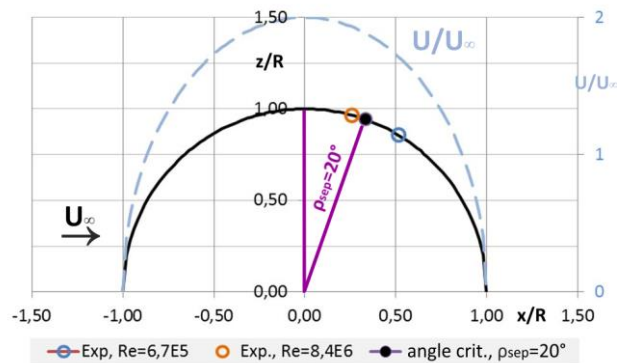


Figure 3: Circular cylinder flow separation points measured in experiments (Roshko [23]) and calculated using the angle criterion with  $\rho_{sep} = 20^\circ$ . The blue dashed line represents the theoretical velocity distribution

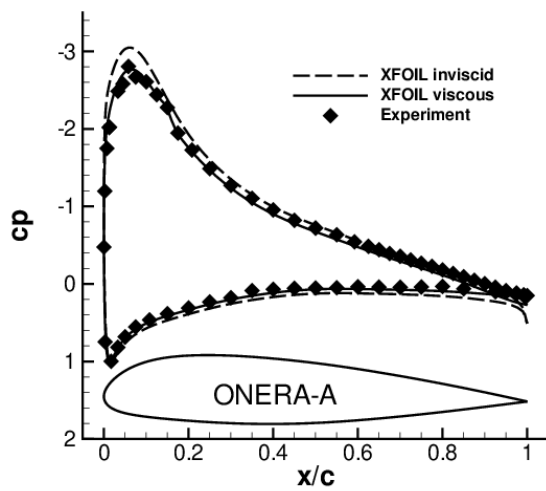
The separation threshold angle  $\rho_{sep}$  can be set by the user. Ahmed [21] and Seddon [22] suggest that a

value of  $\rho_{sep} = 20^\circ$  gives plausible results for bluff bodies. This is confirmed by application of the angle separation criterion to the flow around a circular cylinder and comparison to experimental data from [23] (see Figure 3).

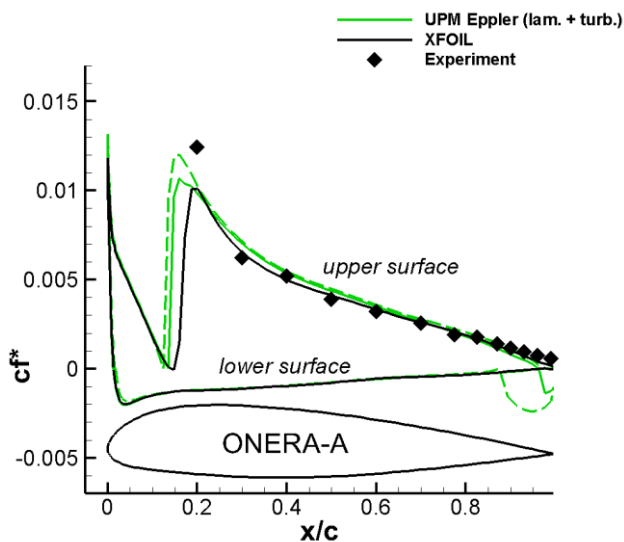
*b) Turbulent Stratford criterion*

The advancing front algorithm was extended to integrate the variables needed by Stratford's turbulent separation criterion [24]. The Stratford constant  $k$ , which defines a threshold value for flow separation, can be set by the user.  $k = 0.39$  is used per default.

The skin friction coefficient is set to zero in the region of separated flow.



(a) pressure distribution



(b) skin friction coefficient, using inviscid (dashed lines) and viscous (solid lines) XFOIL velocity distribution as input

Figure 4: ONERA-A airfoil at  $Ma_\infty = 0.15$ ,  $Re = 2.07 \cdot 10^6$  and  $\alpha = 8.1^\circ$

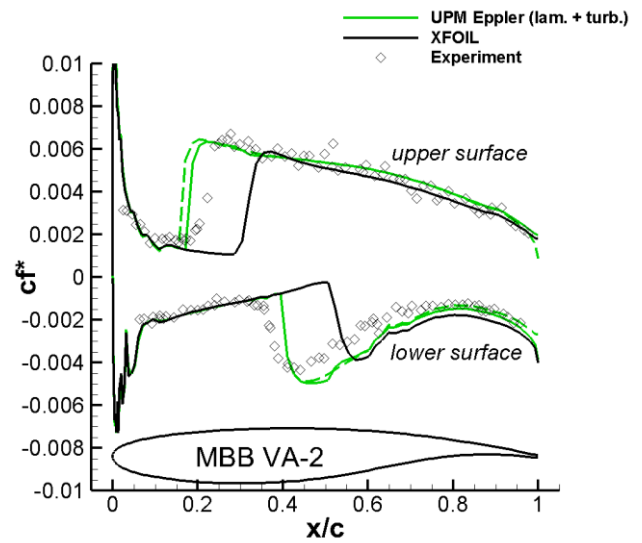
4. Friction loads computation

The loads on each surface patch and the total loads due to skin friction are computed by integrating the local skin friction in direction of the potential flow.

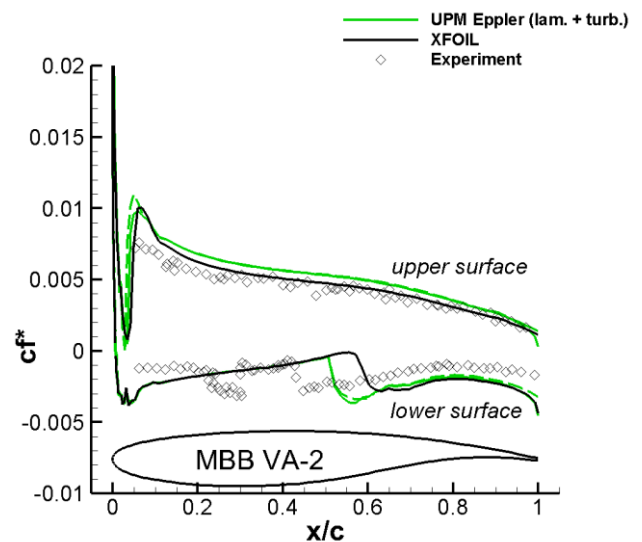
3 RESULTS

3.1 Airfoils

In a first step, the newly implemented integral boundary layer methods were tested and compared in an isolated setup, decoupled from UPM. Therefore, the streamline arc length and velocity distributions from XFOIL [25] calculations were taken as inputs for the



(a)  $Re = 2.0 \cdot 10^6$ ,  $\alpha = 0.0^\circ$



(b)  $Re = 6.0 \cdot 10^6$ ,  $\alpha = 4.0^\circ$

Figure 5: MBB VA-2 airfoil skin friction coefficient at  $Ma_\infty = 0.2$

boundary layer module. In order to determine the influence of boundary layer displacement effects on the solution, each calculation was performed twice, firstly by using the inviscid XFOIL solution as input and secondly by using the viscous XFOIL solution as input, which includes the effect of the boundary layer displacement thickness on the velocity distribution. The results of the newly implemented boundary layer methods were then compared to boundary layer quantities calculated by XFOIL and measured in experiments.

### 3.1.1 ONERA-A

As a first test case the ONERA-A airfoil was selected at an angle of attack  $\alpha = 8.1^\circ$ , a Mach number  $Ma_\infty = 0.15$  and a Reynolds number of  $Re = 2.07 \cdot 10^6$ . For this case experimental data from Gleyzes and Capbern [26] are available, including boundary layer characteristics and skin friction measurements. They show that the flow is fully attached at the upper side near the trailing edge, but close to separation onset. In the calculations, the airfoil geometry was discretized using a total of 160 points. Figure 4 (a) shows the inviscid and viscous pressure distributions calculated by applying XFOIL. The viscous pressure distribution matches the experimental data well, while the inviscid solution deviates slightly from the experiment, especially in the region of the suction peak. Figure 4 (b) shows surface friction coefficients<sup>1</sup> calculated by the UPM Eppler integral boundary layer method together with experimental results from [26] and XFOIL results. The sign of the lower surface skin friction was inverted in order to improve clarity. The results agree very well in the laminar region. Also, in the turbulent region the differences do not exceed the expected range of accuracy. Transition is predicted due to laminar separation and turbulent reattachment by both, XFOIL and the UPM Eppler method. The outcomes using the viscous and inviscid XFOIL results as input for the UPM boundary layer method do not differ considerably in this case. Nevertheless, the predicted laminar separation/transition locations are slightly shifted downstream when taking the viscous velocity distribution as input. This means that the prediction based on the inviscid pressure is more conservative in terms of total drag. The deviation from the XFOIL results is attributed to the fact that XFOIL models laminar separation bubbles with a finite length while the UPM boundary layer module assumes immediate transition after laminar separation. This seems to have the greatest impact in the trailing edge region of the lower side, where the implemented laminar method predicts transition due to laminar separation, while XFOIL's laminar model predicts attached laminar flow until the trailing edge.

<sup>1</sup> all skin friction coefficients were calculated using the local onflow velocity  $U_\infty$

### 3.1.2 MBB VA-2

The supercritical airfoil MBB VA-2 was investigated for two cases at different Reynolds numbers and angles of attack. The onflow conditions were set according to the wind tunnel results from [27] at a low subsonic Mach number of  $Ma_\infty = 0.2$ . The Arnal  $e^n$  approximation by Würz [19] was used for transition prediction. The critical amplification exponent  $n_{crit} = 4.3$  was set to match the given wind tunnel freestream turbulence intensity  $Tu = 0.5\%$ . As before, 160 points were used to discretize the airfoil. Figure 5 shows the calculated and measured skin friction coefficients for the two investigated cases. Again, boundary layer analysis results based on the inviscid XFOIL solutions are depicted using dashed lines and the  $c_f$  values of the lower surface are negated. For the case at  $\alpha = 0^\circ$  (Figure 5 (a)), similar conclusions as for the ONERA-A airfoil can be drawn. The computation methods and the experiment agree well in the laminar flow region. This is attributed to the fact that the airfoil is designed to produce a pressure distribution with a flat plateau, which resembles the flat plate conditions. The transition locations predicted by the implemented laminar method in conjunction with the selected transition model are in good accordance with the experimental data, especially on the lower side. Again, the difference between the results based on the inviscid and the viscous XFOIL results are marginal. They are only noticeable in the slight backward shift of the upper side transition location when viscous effects are included in the velocity distributions. A much greater difference is observed when looking at the transition locations predicted by XFOIL. They are around 10 – 15% downstream when compared to the experiment and the other methods, even though an identical value was used for  $n_{crit}$ . The discrepancies are probably caused by the differences in the transition prediction models used. In the turbulent region, the computed skin friction curves lie within the bandwidth of the sample points of the experiment for the upper surface. Regarding the lower surface, the computed solutions overpredict the skin friction slightly when compared to the experiment. When looking at the  $\alpha = 4^\circ$  case, it makes almost no difference whether the viscous or the inviscid velocity distribution is taken as input for the boundary layer methods. This behavior is probably caused by the significantly larger Reynolds number of  $Re = 6.0 \cdot 10^6$ , which implies thinner boundary layers and thus reduces the displacement effect on the potential flow solution. Otherwise, the computed and measured skin friction coefficients are in good agreement even for this case.

### 3.2 Tapered Wing

After successful validation of the implemented integral boundary layer methods for airfoils using external velocity distributions from XFOIL as input, the boundary layer module was fully integrated into UPM. For all following simulations, UPM's internal panel geometry and potential flow solution were used as inputs for the boundary layer routines. Various simple wing geometries were used as test cases for the newly implemented routines [14]. Here, only results for a tapered wing with taper ratio  $\lambda = 0.5$  are shown. The wing had a root chord length  $c = 1$  and the halfspan  $b = 4$ . It was untwisted and employed the NACA0012 airfoil. The surface of each half wing was discretized by a total of 100 panels in chordwise direction and 11 panels in spanwise direction. The set flow conditions were  $Ma_\infty = 0$ ,  $Re = 4.0 \cdot 10^6$  and  $\alpha = 5^\circ$ . VSAERO [18] results for the wings were selected as a reference because it is a well-established steady coupled 3D panel and boundary layer code which has been successfully used for several wing and fuselage pre-design activities at DLR. Nevertheless, there were slight differences between the UPM and the VSAERO calculation setups:

- The VSAERO wings were closed at the tips by a planar panel patch while the wings modeled in UPM had open tips.
- In VSAERO a planar prescribed wake was used while the UPM wake rolled up due to the unsteady simulation.
- In VSAERO the boundary layer analysis was performed on streamlines starting at seeding points at the trailing edge center point of each segment, while UPM performed stripwise analyses along the collocation points of the panels of each segment.

Figure 6 depicts the UPM and VSAERO results for the tapered wing. In the lift coefficient plot Figure 6 (b), only the inviscid forces are shown because the lift component due to friction is negligible. The skin friction distributions of VSAERO and the UPM boundary layer methods in Figure 6 (a) show a good qualitative agreement, even though the transition position calculated by VSAERO for the lower side is located slightly upstream of the UPM result and the  $c_f$  predicted by the UPM boundary layer method is slightly higher. Figure 6 (c) shows the total drag coefficient and its component due to skin friction calculated by VSAERO and UPM. The differences in the computed friction drag are very small, relatively even smaller than for the total drag. Large deviations in the tip region due to the different wing tip cap modeling are observed. For the tapered wing, the local Reynolds number decreases linearly from root to tip. The results encourage assuming that Reynolds effects are captured correctly by the UPM boundary layer method.

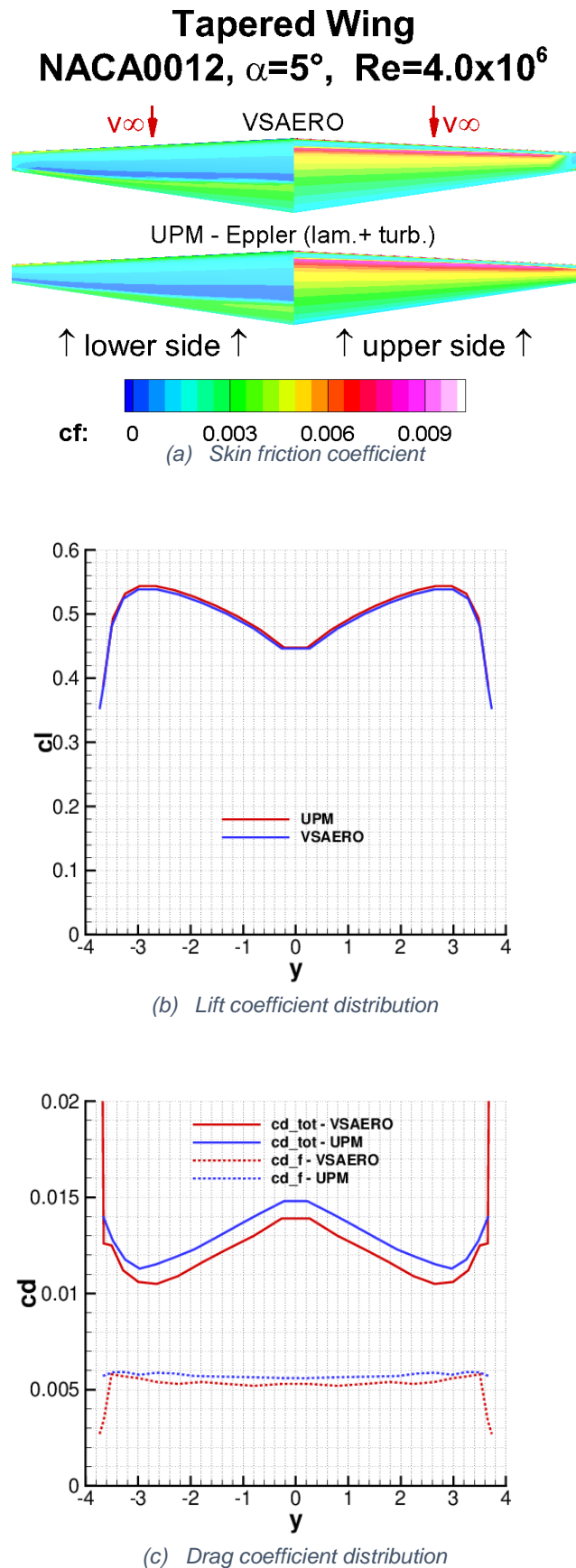


Figure 6: Tapered wing at  $Re = 4.0 \cdot 10^6$ ,  $\alpha = 5^\circ$

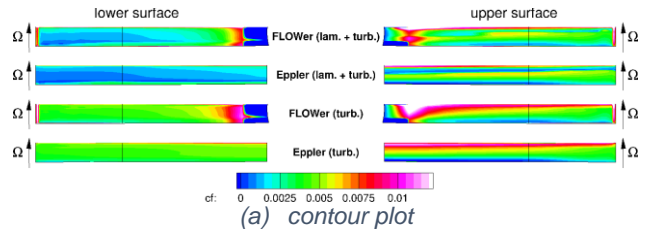
### 3.3 Rotor 7A in Hover

The 7A rotor in hover was selected to validate the implemented approximate boundary layer methods for rotors. Wind tunnel and whirltower measurements [28] are available for this rotor. Furthermore, RANS calculation results using DLR's in-house RANS codes FLOWer and TAU were available as reference solutions.

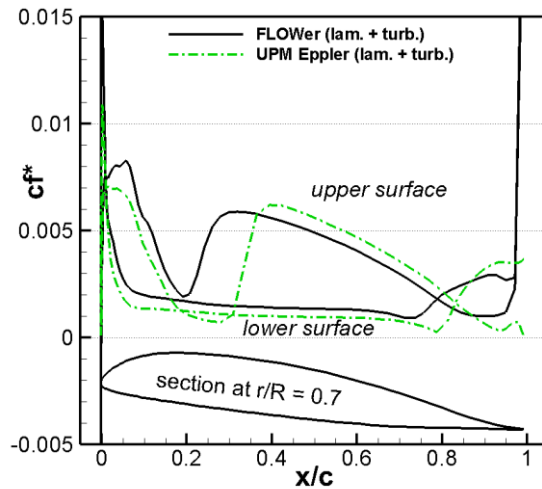
The simulated model rotor has a radius of  $2.1m$  and a chord length of  $0.14m$ . The considered test case had a tip Mach number  $Ma_{tip} = 0.617$ . The surface of each rotor blade was discretized by 98 panels in chordwise direction and 17 panels in radial direction. The CFD surface meshes used twice the resolution for both, chordwise and spanwise, discretizations. For the unsteady UPM simulations a total of 8 rotor revolutions were computed for each data point.

Figure 7 depicts calculated skin friction distributions for  $5.97^\circ$  collective pitch. The upper two solutions shown in Figure 7 (a) were computed including boundary-layer transition prediction, the lower two solutions were computed assuming fully turbulent flow. The CFD and UPM results in the outer blade region agree well for both, transitional and fully turbulent setups. The chordwise skin friction coefficient distributions at  $r/R = 70\%$  shown in Figure 7 (b) and (c) give further insight into the results. The transition point predicted by FLOWer on the upper surface is located around 10% upstream of the UPM results. It is probably caused by differences in the pressure distribution or by different assumptions regarding the turbulence level. On the lower surface the transition points match very well, even though the laminar skin friction calculated by FLOWer and UPM have a small offset. In the turbulent region UPM and FLOWer agree well. The accordance is surprisingly good when considering the many simplifications inherent to the UPM simulations.

The rotor performance results of four collective pitch angles are compiled in Figure 8. The thrust coefficients calculated by UPM agree with the CFD solutions. For most operating points UPM predicts a marginally lower thrust coefficient. The discrepancy of the two experimental datasets is much larger than the differences observed in the simulated results. Only the inviscid UPM result is plotted because the influence of the friction forces on thrust can be neglected. The power coefficient predicted by UPM when using the boundary layer methods with transition prediction (Arnal  $e^n$  approximation by Würz [19] with  $n_{crit} = 9$ ) matches the experiment, especially for the smaller collective pitch angles. But when considering the slight overprediction of thrust for the same experiment, a noticeable overprediction of the required power is expected, as it is the case for the FLOWer result. The lower power predicted by UPM may be explained by the missing form drag component, but could also originate from a difference in the induced drag calculated by CFD and UPM.

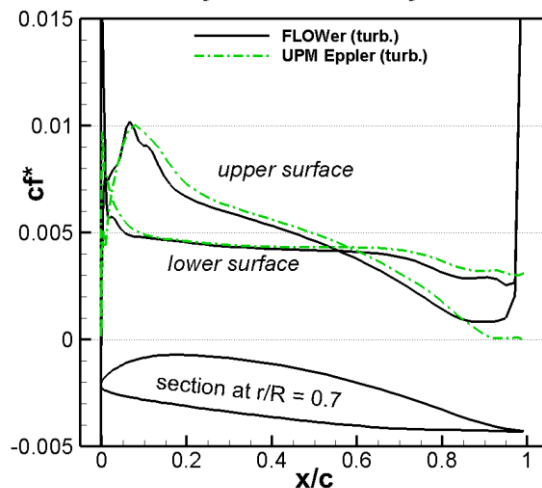


**laminar/turbulent analysis incl. transition**



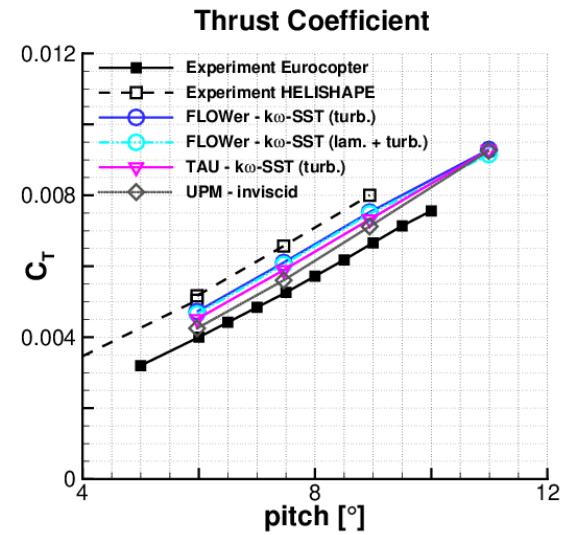
(b) section  $r/R=0.7$  laminar/turbulent analysis results including transition prediction

**fully turbulent analysis**

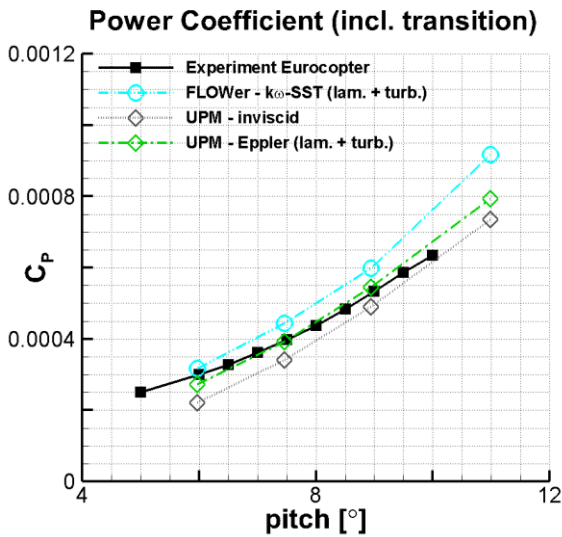


(c) section  $r/R=0.7$  fully turbulent analysis results

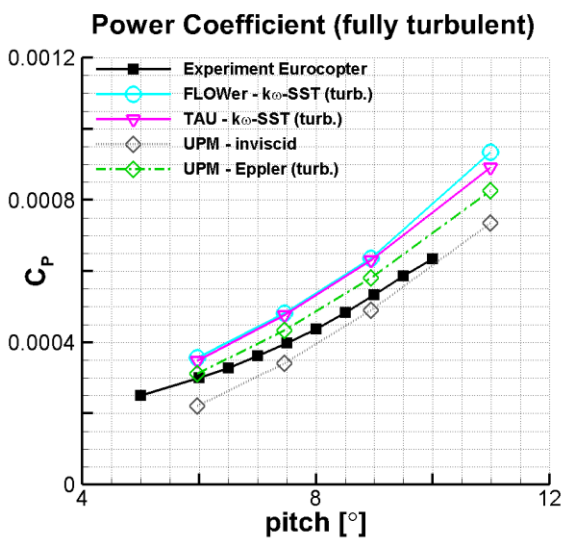
Figure 7: Rotor 7A skin friction coefficient, collective pitch  $5.97^\circ$



(a) thrust coefficient



(b) power coefficient - laminar/turbulent analysis results including transition prediction



(c) power coefficient - fully turbulent analysis results

Figure 8: Rotor 7A simulated and measured performance

As expected, the calculated power is shifted upwards for all fully turbulent simulations, when compared to the respective results including transition. The delta between UPM and FLOWer results stays approximately the same when comparing the fully turbulent polar to the polar with transition. The fact that the delta gets larger for larger pitch angles is an indication that the missing form drag increases at larger collective pitch angles.

### 3.4 Fuselages

The simplified boundary layer analysis method described in section 2.3.2 was tested for two isolated fuselages.

#### 3.4.1 ROBIN

Figure 9 depicts surface pressure and friction results of the implemented simplified boundary layer analysis for the isolated ROBIN fuselage [29] together with VSAERO [18] results. The fuselage was calculated at an angle of attack  $\alpha = 0^\circ$  at Mach number  $Ma_\infty = 0.1$  and Reynolds number  $Re = 1.6 \cdot 10^6$ . The same surface discretization was used for both the UPM and the VSAERO simulations. The full model consisted of 6,800 quadrilateral panels for the main body and 1,054 panels for the pylon. The panels were arranged in two structured patches. The inviscid solutions of the two codes match very well as seen in the pressure distributions in Figure 9 (a).

The skin friction coefficient is plotted in in Figure 9 (b). For the VSAERO boundary layer analysis transition was tripped right after the stagnation points in order to obtain results which are comparable to the fully turbulent approach that is implemented in UPM. VSAERO performs integral boundary layer analyses along surface streamlines, for which the seed points are specified by the user. It implements integral boundary layer methods by Thwaites/Curle [30], [31] (laminar) and Nash/Hicks [32] (turbulent). The analysis stops if flow separation is predicted. The results are then mapped back from the streamline points to the surface panels.

This test case is a challenging task for the streamline arc length computation procedure because there are two stagnation points. Nevertheless, the advancing front algorithm worked robustly. The skin friction calculated by VSAERO and UPM show qualitatively similar distributions. But the flat plate analogy relation seems to overestimate skin friction on a large portion of the surface, returning a conservative value for the total friction drag when compared to VSAERO.

Both, the angle criterion with a threshold angle  $\rho_{sep} = 20^\circ$  and the turbulent Stratford criterion with  $f = 0.39$  were applied for estimation of flow separation areas in UPM. The predicted flow separation line is highlighted by a thick red contour line in Figure 9 (b). The flow separation area predicted by the angle criterion

at the back of the pylon is considerably larger than the one predicted by VSAERO. But, in contrast to VSAERO, the separation state is not propagated downstream along the streamlines. The separation line predicted by the Stratford criterion lies between the results of VSAERO and the angle criterion.

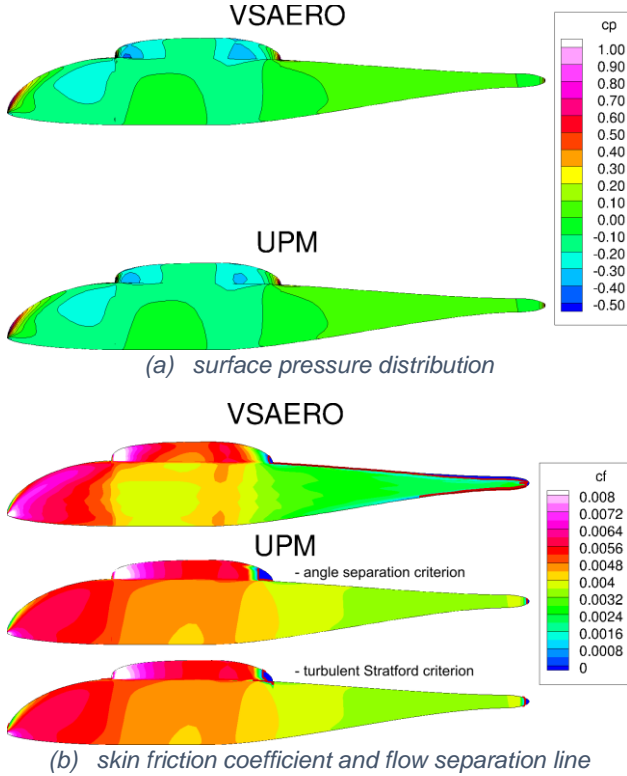


Figure 9: ROBIN fuselage at  $\alpha = 0^\circ$

### 3.4.2 ROBIN-mod7

A similar comparison was made for the ROBIN-mod7 body [33] without pylon. The onflow conditions corresponded to those of the previous case. The fuselage consisted of a single structured patch with 6,400 quadrilateral panels. Figure 10 shows the computed surface pressure and skin friction results. The modified geometry is less streamlined when compared to the original ROBIN body, thus giving rise to a large flow separation area in the backward facing region. This is observed in both VSAERO and UPM results (Figure 10 (b)). Again, the angle criterion with a threshold angle  $\rho_{sep} = 20^\circ$  and the Stratford criterion with  $f = 0.39$  were used for estimation of the separation area in UPM. As for the previous case, the local skin friction calculated by UPM is mostly larger than the corresponding VSAERO result and the separation line calculated using the angle criterion begins further upstream when compared to the VSAERO prediction. The separation line of the Stratford criterion is closer to the VSAERO result in the backdoor area, but extends further upwards in the tail boom root region.

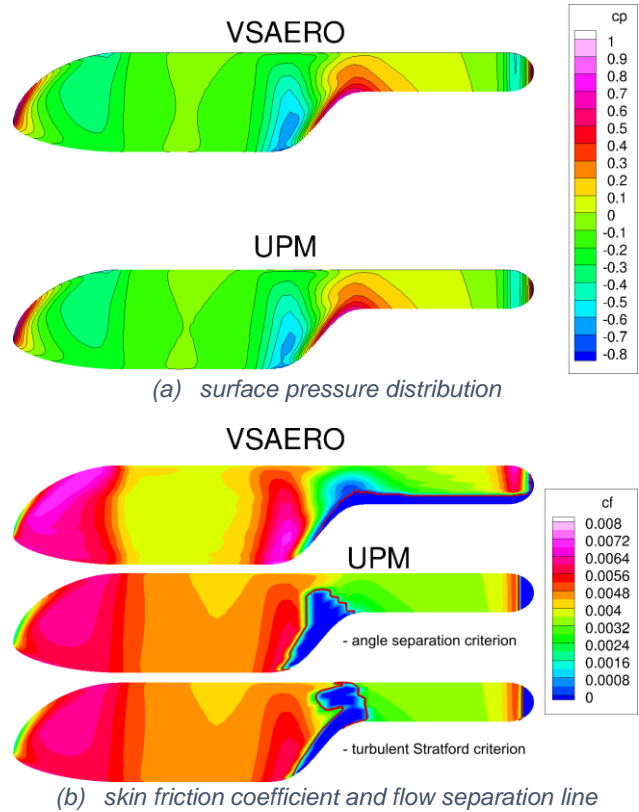


Figure 10: ROBIN-mod7 fuselage at  $\alpha = 0^\circ$

### 3.5 GOAHEAD Complete Helicopter

The GOAHEAD configuration was selected to validate UPM for complete helicopter simulations. The wind tunnel model consists of a 4.1m long fuselage resembling the NH90 transport helicopter at a scale of 1:3.88. It was combined with the four blade ONERA 7AD rotor with 2.1m radius and a scaled BO105 tail rotor with 0.383m radius. An extensive experimental database was generated within the European project GOAHEAD where the model was tested in the Large Low-speed Facility (LLF) of the German-Dutch joint wind tunnels. The reader is referred to [34] for a detailed description of the model and the acquired data.

Table 1: Flow Conditions and model parameters

GOAHEAD test case 3-4 (cruise / high-speed tail-shake)			
GOAHEAD data point	$D_{pt}$	396	[-]
Wind tunnel Mach number	$Ma_\infty$	0.204	[-]
Fuselage pitch	$\alpha_f$	-2.5	[°]
MR shaft inclination	$\alpha_s$	-7.5	[°]
MR tip Mach number	$Ma_{tip,MR}$	0.617	[-]
TR tip Mach number	$Ma_{tip,TR}$	0.563	[-]

The cruise test case (Table 1) was selected for the verification and validation of UPM, focusing on the results of the newly implemented unsteady surface pressure calculation routines.

The UPM simulation setup contained the main and the tail rotor (MR, TR) along with the fuselage, horizontal and vertical stabilizers (HS, VS), a simplified main rotor hub fairing and the strut. Additionally, the wind tunnel side walls and ceiling were modelled using source/sink panels and the floor was modelled by a mirror plane (see Figure 11).

The surface panels were generated using digitized CAD data of the original wind tunnel model. The rotor blades were cut in the root region and the gap between fuselage and rotor hub was closed. The upper part of the vertical stabilizer was simplified by omitting the tail rotor gearbox. TR shaft and hub were also neglected.

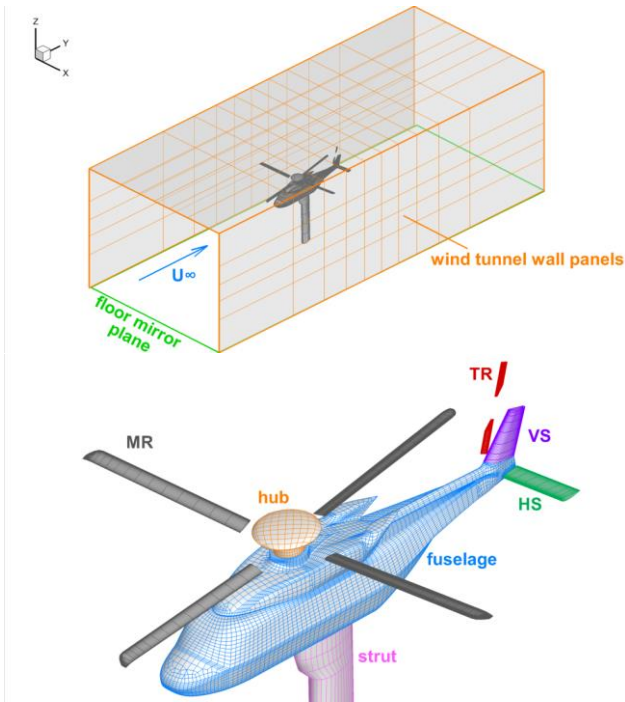


Figure 11: Top: Model of the wind tunnel walls. Bottom: Surface paneling of the various components

Table 2 lists the number of surface panels used to discretize each component.

Table 2: Number of panels of the various components in the UPM simulation. Lifting surfaces are marked with \*

component	# blades	# panels			total
		spanwise	chordwise		
MR*	4	16	80		5120
TR*	2	8	48		768
HS*	1	10	66		660
VS*	1	8	66		528
Fuselage					9055
Hub					820
Strut					252
W/T					160
Complete					17363

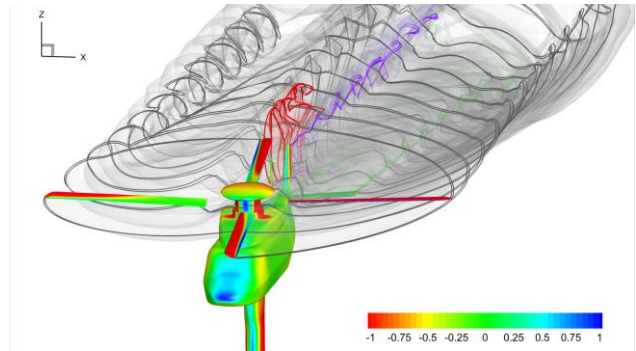


Figure 12: Surface pressure coefficient and wake visualization after three complete MR revolutions

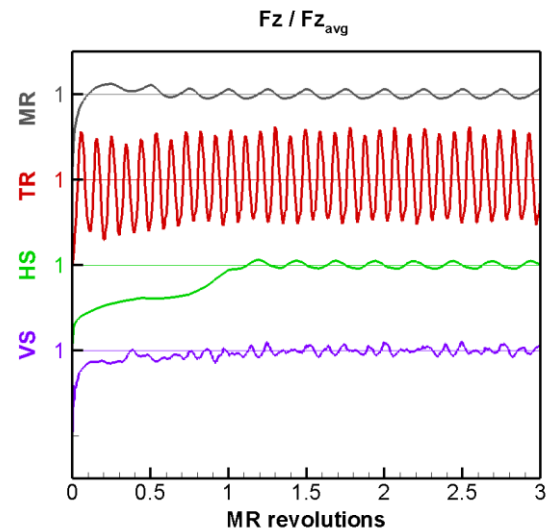


Figure 13: Time history of normalized z-force in body coordinates for all lifting components. 1 corresponds to the final averaged z-force of the respective component

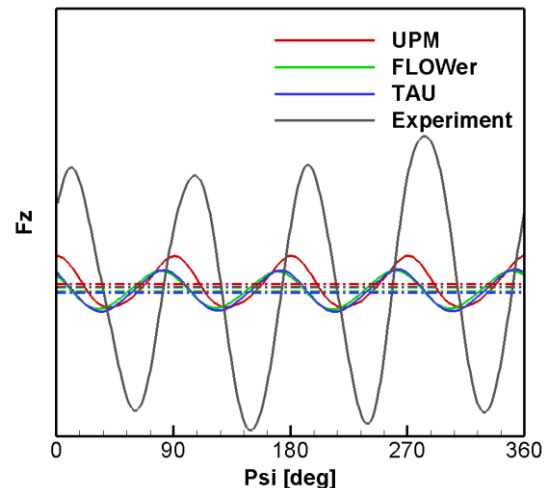


Figure 14: Calculated and measured main rotor z-force. Dash-dotted lines denote mean values

UPM was set up to simulate a total of 3 MR revolutions at 2° MR azimuth steps. The tip vortex roll-up model was deactivated. Instead, the full-span wake

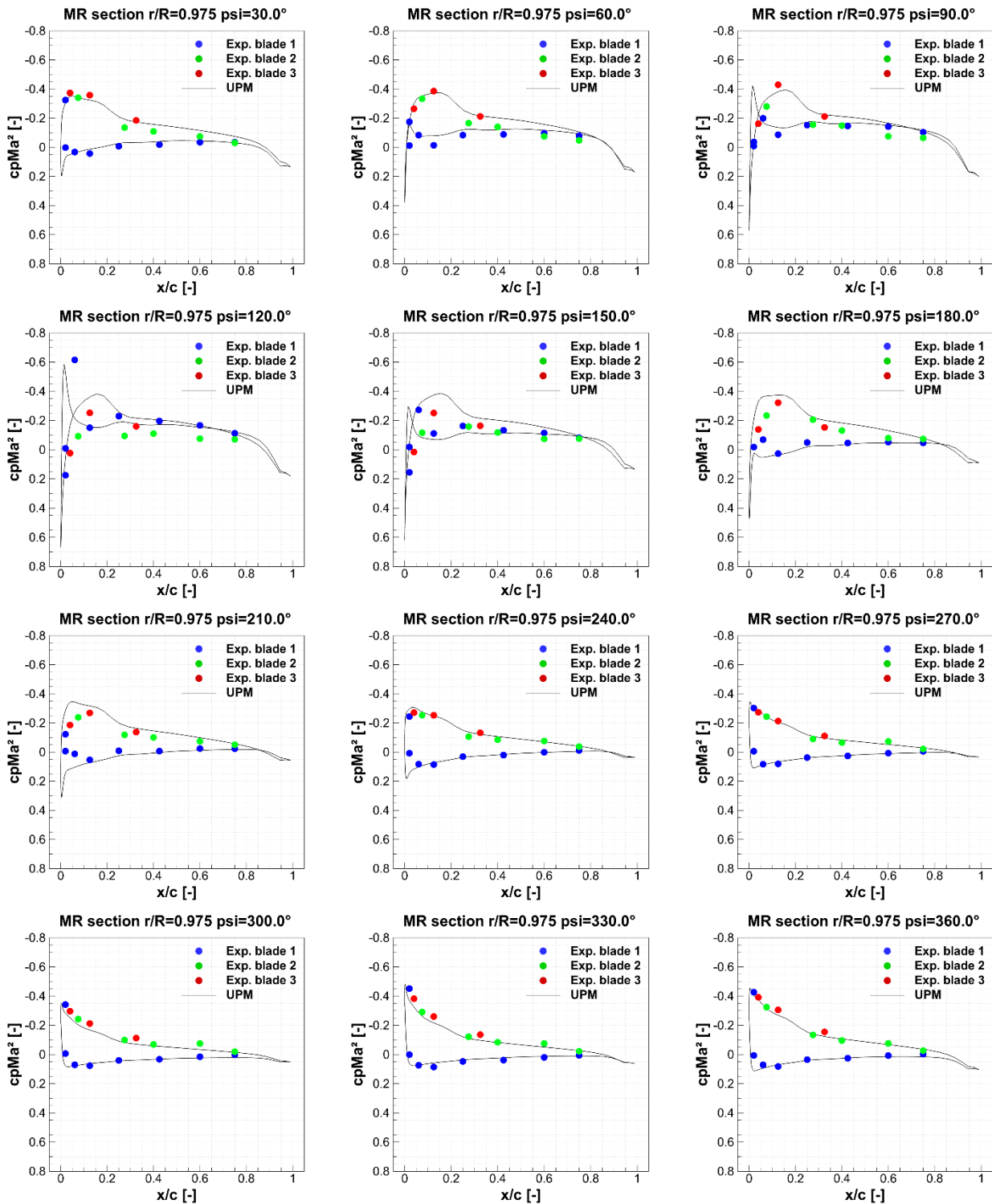


Figure 15: MR unsteady surface pressure at blade section  $r/R = 97.5\%$

was used with a vortex core radius of 80% of the blade chord. The TR wake was cut off after 3 TR revolutions. Sectional Prandtl-Glauert compressibility correction was activated. Control angles and rigid blade motion were prescribed from a preceding calculation with the Helicopter Overall Simulation Tool HOST [35]. Only the constant term and the 1<sup>st</sup> harmonic of the flapping and lead-lag motions were

considered. Elastic blade deformation was neglected. The total sequential run time of such a UPM simulation is approximately 30 hours on a modern workstation using one CPU.

Figure 12 shows the instantaneous surface pressure coefficient contours and the wake geometry at the last time step of the simulation.

The time history of the z-forces in body coordinates depicted in Figure 13 suggests that a quasi-periodic solution is already obtained after 1.5 revolutions for all relevant components.

Figure 14 compares the calculated main rotor z-force history of the last revolution with measured data and CFD results from [36]. The mean UPM force matches the experimental value very well, when considering that the control angles were prescribed without any further coupling or trimming. Phase and amplitude of the UPM signal are in the range between the CFD results and the experiment.

Figure 15 shows the pressure distributions at a main rotor blade section very close to the tip ( $r/R = 97.5\%$ ) during a complete rotor revolution. For a large range of azimuth angles the agreement with the measured data is comparable to that of CFD simulations (e.g. [36]). Merely in the azimuth range between  $90^\circ$  and  $210^\circ$  larger deviations are observed. These can be partly attributed to the missing aeroelastic trim in the UPM simulation. Additionally, the simple Prandtl-Glauert compressibility correction lacks accuracy in modeling the compressibility effects at the high Mach numbers in the tip region of the advancing side. Furthermore, the flow in the tip region is highly three-dimensional at azimuth angles around  $180^\circ$ . Here, the flow may separate at the leading and outer edges of the parabolic blade tip and thus the assumption that the wake is only released at the trailing edge can be wrong. More inboard the impact of these effects on the solution decreases rapidly and a better accordance between experiment and UPM results is observed, as can be seen in Figure 16.

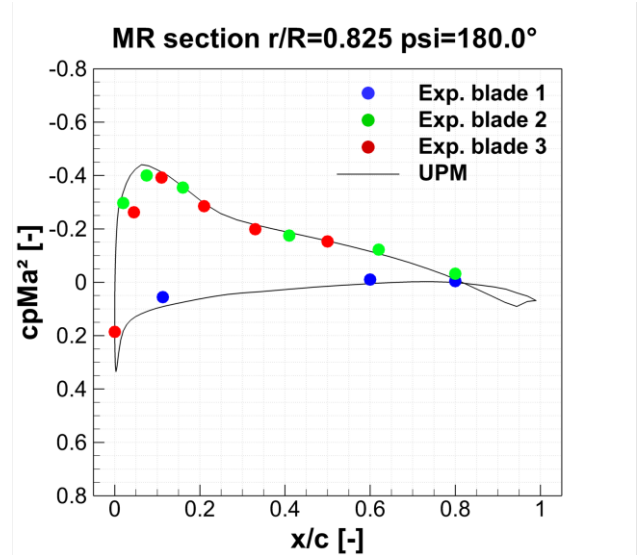


Figure 16: MR unsteady surface pressure at  $r/R=82.5\%$ ,  $\psi=180^\circ$

The averaged surface pressure distribution on the fuselage is depicted in Figure 17. Measured data of the steady and averaged data of the unsteady pressure sensors are included as octahedrons and spheres colored using the same color map as the surface contours. Overall, the computed and measured pressures match well. Nevertheless, a noticeable deviation is observed in the backdoor region, which becomes apparent in Figure 18. Here, the pressure recovery is overestimated by UPM, because pressure losses cannot be modelled by the non-lifting body approach used for the fuselage. PIV measurements and CFD results [37] show that flow separates at the edges of the rear-facing ramp and rolls up in two counter-rotating vortices which affect the flow around

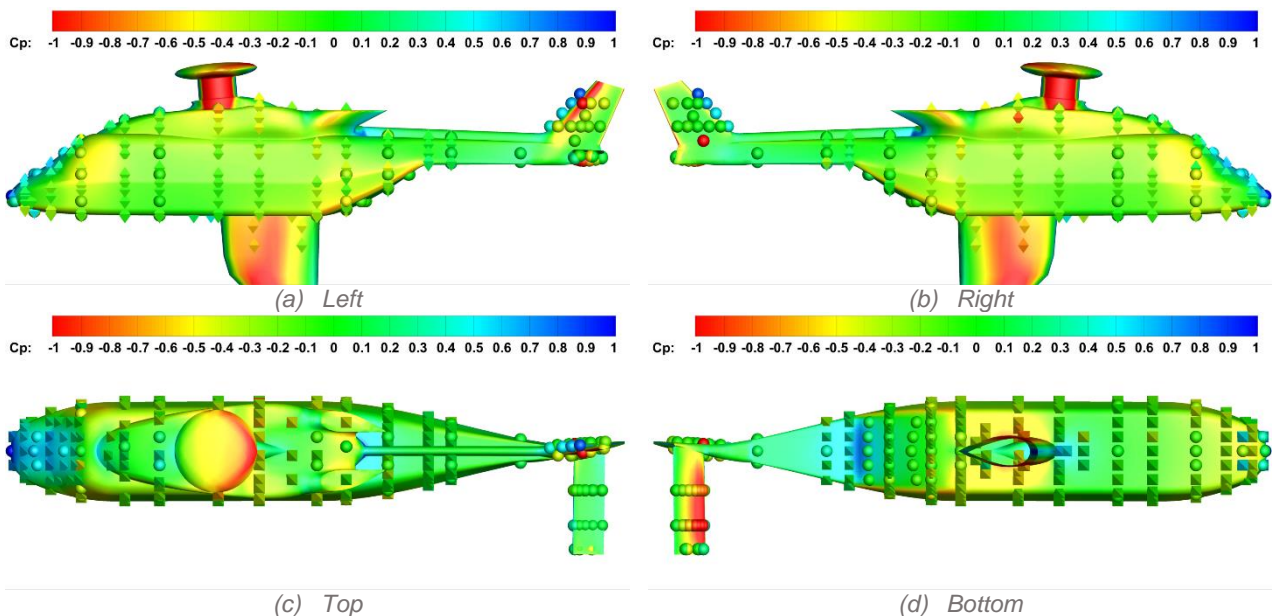


Figure 17: Computed averaged surface pressure distribution compared to measured pressures (octahedrons=steady pressure sensor data, spheres=averaged unsteady pressure sensor data)

the backdoor and the lower tail boom region considerably.

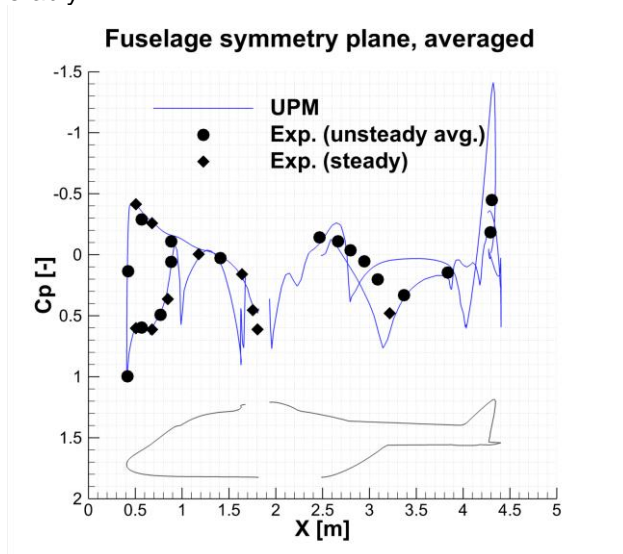


Figure 18: Comparison of computed and measured averaged pressure distribution in the symmetry plane of the GOAHEAD fuselage

Figure 19 shows computed and measured unsteady pressures at selected transducer locations over the main rotor azimuth angle. Almost all computed curves show a good qualitative agreement with the measured data. Especially the phase and the shape of the pressure signals match the experiment for most transducers. In the front part of the fuselage (transducers A06-A20) the amplitude of the pressure fluctuations is underpredicted by UPM. At the transducer A20 the constant part of the pressure signal is also slightly underestimated. Possible causes for this behavior are the missing trim and the deviations of blade loads in the region around  $180^\circ$  azimuth, which were already observed in Figure 15. A large deviation in the constant part of the pressure is observed for the transducer K22, located at the fuselage backdoor. It shows that the overestimated pressure recovery observed in Figure 18 does not arise from unsteady pressure fluctuations. The UPM results for the sensors located at the tail boom (K41-K45) match the experiment well. Only at sensor K45 the signal shape and amplitude differ noteworthy from the measured signal. On closer examination of the calculated wake in this region, it can be noticed that the main rotor wake gets distorted when penetrating the exhaust deflector located upstream of this sensor and thus causes a noisy pressure footprint with a smaller amplitude and a less distinct 4/rev signal.

## 4 CONCLUSION

Two major steps of the modernization and extension process of DLR's unsteady panel and free-wake code UPM were taken.

Firstly, approximate boundary layer analysis methods for lifting and non-lifting bodies were implemented and validated for isolated airfoils, wings, a rotor and two fuselages. Most lifting surface analysis results were in accordance with experimental data and reference solutions. The calculated friction drag is sufficiently accurate for the envisaged applications and the analysis methods can predict laminar-turbulent transition due to TS-instabilities. Nevertheless, the implementation as a post-processing step is not able to capture viscous-inviscid interaction effects, e.g. form drag due to the displacement of the potential flow by the boundary layers. The simplified analysis method for fuselages leads to reliable outcomes, even though the accuracy lags behind the one of the stripwise analysis for lifting surfaces. These limitations should be taken into account when applying the approximate boundary layer methods.

Secondly, a new method for the calculation of unsteady pressures on arbitrary bodies was implemented and a complete helicopter simulation of the GOAHEAD configuration in cruise was performed in order to validate the new method. The computed unsteady surface pressures showed a good agreement with experimental data. But here, too, individual flow regions reveal the limits of the underlying theory.

As a next step, the approximate boundary layer analysis methods will be validated for a complete helicopter simulation. Then, the modernization and extension process of UPM will focus on coupling interfaces, performance optimization and parallelization.

## ACKNOWLEDGMENT

The project this report is based on was funded by the German Federal Ministry for Economic Affairs and Energy under grant number 20H1501B. The responsibility of this publication lies with the author.

### Copyright Statement

The authors confirm that they, and/or their company or organization, hold copyright on all of the original material included in this paper. The authors also confirm that they have obtained permission, from the copyright holder of any third party material included in this paper, to publish it as part of their paper. The authors confirm that they give permission, or have obtained permission from the copyright holder of this paper, for the publication and distribution of this paper as part of the ERF proceedings or as individual offprints from the proceedings and for inclusion in a freely accessible web-based repository.

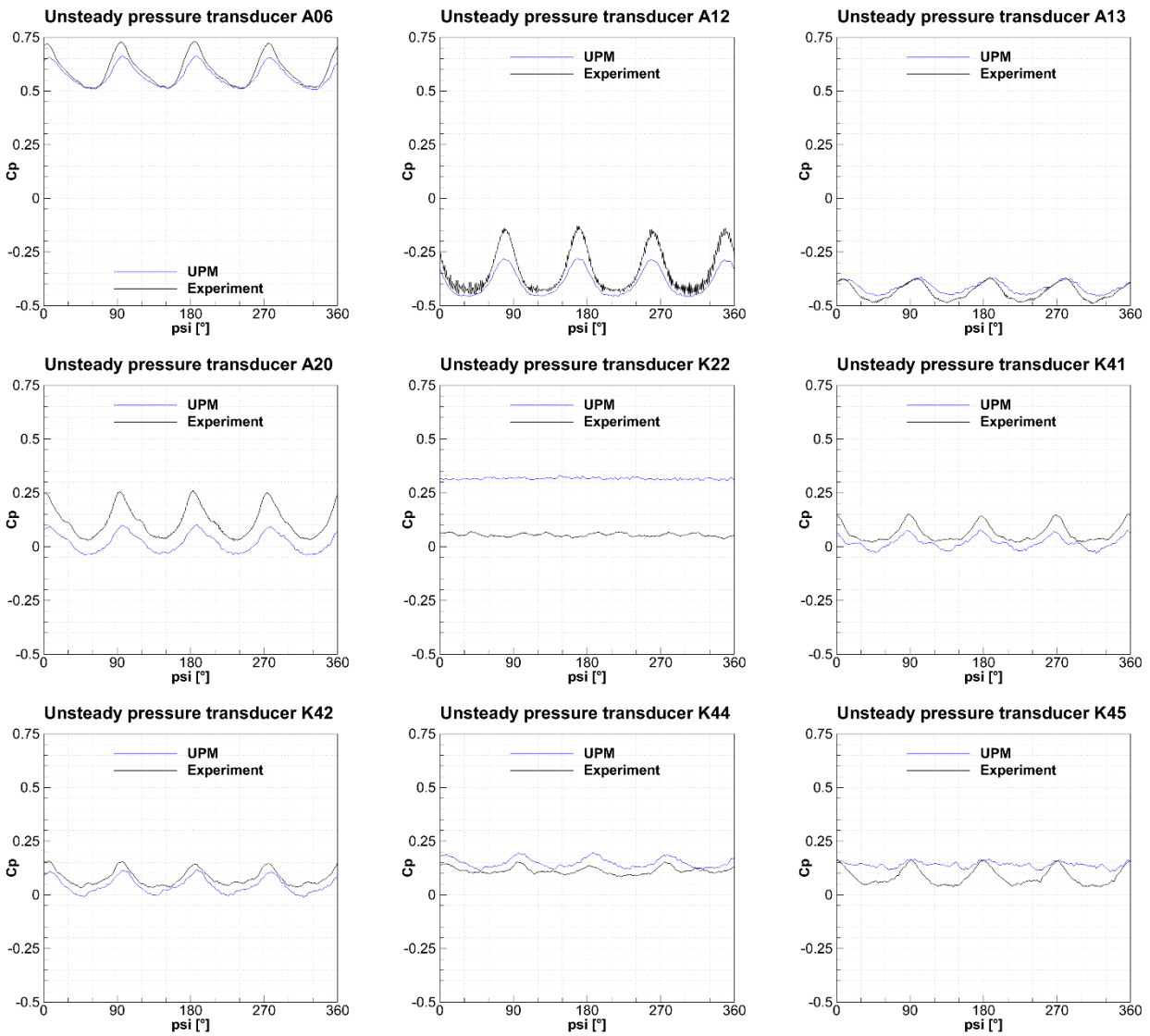
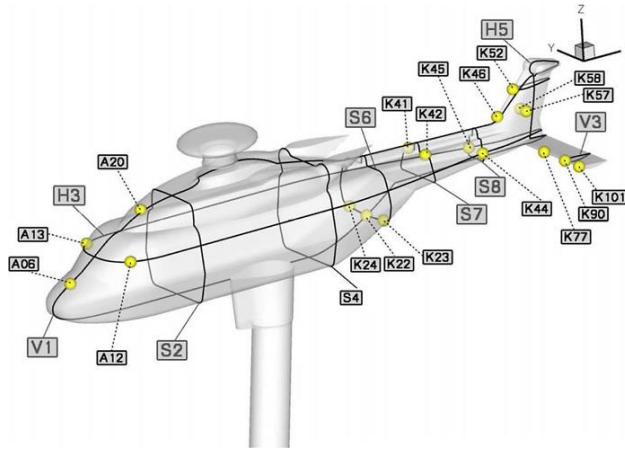


Figure 19: Fuselage pressure sensor locations (top) and pressure time series plots for 9 unsteady pressure transducer positions

## REFERENCES

- [1] J. Yin and S. R. Ahmed, "Helicopter Main-Rotor/Tail-Rotor Interaction," *Journal of the American Helicopter Society*, vol. 4, pp. 293-302, 2000.
- [2] S. R. Ahmed and V. T. Vidjaja, "Unsteady Panel Method Calculation of Pressure Distribution on BO105 Model Rotor Blades," *Journal of the American Helicopter Society*, vol. 43, pp. 47-56, 1998.
- [3] J. Yin, A. Stuermer and M. Aversano, "Aerodynamic and Aeroacoustic Analysis of Installed Pusher-Propeller Aircraft Configurations," *Journal of Aircraft*, vol. 49, pp. 1423-1433, 2012.
- [4] M. Wentrup, J. Yin, P. Kunze, T. Streit, J.-H. Wendisch, T. Schwarz, J.-P. Pinacho, K. Kicker and R. Fukari, "An overview of DLR compound rotorcraft aerodynamics and aeroacoustics activities within the CleanSky2 NACOR Project," in *AHS International 74th Annual Forum & Technology Display*, Phoenix, 2018.
- [5] G. Wilke, "Aerodynamic Optimization of Helicopter Rotor Blades using Variable Fidelity Methods," Germany, 2017.
- [6] P. Kunze, "Evaluation of an unsteady panel method for the prediction of rotor-rotor and rotor-body interactions in preliminary design," in *41st European Rotorcraft Forum*, Munich, 2015.
- [7] M. Schmid, "Simulation of Helicopter Aerodynamics in the Vicinity of an Obstacle using a Free Wake Panel Method," in *43rd European Rotorcraft Forum*, Milan, 2017.
- [8] M. Rinker, T. Ries, M. Embacher, G. Uhl and M. Hajek, "Simulation of Rotor-Empennage Interactional Aerodynamics with Comparison to Experimental Data," in *AHS International 75th Annual Forum & Technology Display*, Philadelphia, 2019.
- [9] J. L. Hess and A. M. O. Smith, "Calculation of potential flow about arbitrary bodies," *Progress in Aerospace Sciences*, vol. 8, pp. 1-138, 1967.
- [10] G. Rahier and Y. Delrieux, "Blade-Vortex Interaction Noise Prediction Using a Rotor Wake Roll-Up Model," *Journal of Aircraft*, vol. 34, pp. 522-530, 1997.
- [11] T. F. Brooks, C. L. Burley, D. D. Boyd and J. R. Jolly, "Aeroacoustic codes for rotor harmonic and BVI noise - CAMRAD.Mod1/HIRES," in *2nd AIAA/CEAS Aeroacoustics Conference*, 1996.
- [12] S. Kinnas, C.-Y. Hsin and D. Keenan, "A Potential Based Panel Method for the Unsteady Flow Around Open and Ducted Propellers," in *Eighteenth Symposium on Naval Hydrodynamics*, Washington, 1991.
- [13] D. A. Wachspress, T. R. Quackenbush and A. H. Boschitsch, "Vortex Methods for the Computational Analysis of Rotor/Body Interaction," in *American Helicopter Society 56th Annual Forum*, Virginia Beach, Virginia, USA, 2000.
- [14] P. Kunze, "Approximate Boundary Layer Methods for a 3D Panel Code for Helicopter Simulations," in *19th ONERA-DLR Aerospace Symposium (ODAS 2019)*, Meusson, France, 2019.
- [15] R. Eppler, "Praktische Berechnung laminarer und turbulenter Absauge-Grenzschichten," *Ingenieur-Archiv*, vol. 32, pp. 221-245, 7 1963.
- [16] R. Eppler, "Turbulent Airfoils for General Aviation," *Journal of Aircraft*, vol. 15, pp. 93-99, 2 1978.
- [17] R. Eppler and D. M. Somers, "A computer program for the design and analysis of low-speed airfoils," NASA Langley Research Center, Hampton, VA, United States, 1980.
- [18] J. Nathman, "VSAERO User's Manual, Version 7.02," Analytical Methods Inc., Redmond, 2007.
- [19] W. Würz, "Hitzdrahtmessungen zum laminar-turbulenten Strömungsumschlag in anliegenden Grenzschichten und Ablöseblasen sowie Vergleich mit der linearen Stabilitätstheorie und empirischen Umschlagskriterien," 1995.
- [20] H. Schlichting, E. Krause, H. J. Oertel and K. Gersten, *Grenzschicht-Theorie*, Heidelberg: Springer, 2006.
- [21] S. R. Ahmed, G. Ramm and G. Faltin, "Some Salient Features of the Time-Averaged Ground Vehicle Wake," 1984.
- [22] J. Seddon, "Aerodynamics of the helicopter rear fuselage upsweep," in *8th European Rotorcraft Forum*, Aix-en-Provence, France, 1982.
- [23] A. Roshko, "Experiments on the flow past a circular cylinder at very high Reynolds number," *Journal of Fluid Mechanics*, vol. 10, pp. 345-356, 1961.
- [24] B. S. Stratford, "The Prediction of Separation of the Turbulent Boundary Layer," *Journal of Fluid Mechanics*, vol. 5, pp. 1-16, 1959.
- [25] M. Drela, "Xfoil: An analysis and design system for low Reynolds number airfoils," in *Low Reynolds Number Aerodynamics*, T. J. Mueller, Ed., Berlin Heidelberg, Springer, 1989, pp. 1-12.
- [26] C. Gleyzes and P. Capbern, "Experimental study of two AIRBUS/ONERA airfoils in near stall conditions. Part I: Boundary layers," *Aerospace Science and Technology*, vol. 7, pp. 439-449, 9 2003.

- [27] D. J. Monson, G. G. Mateer and F. R. Menter, "Boundary-Layer Transition and Global Skin Friction Measurement with an Oil-Fringe Imaging Technique," SAE International, 1993.
- [28] K.-J. Schultz, W. Splettstoesser, B. Junker, W. Wagner, E. Schoell, E. Mercker, K. Pengel, G. Arnaud and D. Fertis, "A parametric windtunnel test on rotorcraft aerodynamics and aeroacoustics (Helishape) – test procedures and representative results," *The Aeronautical Journal*, vol. 101, pp. 143-154, 1997.
- [29] C. Freeman und R. E. Mineck, „Fuselage Surface Pressure Measurements of a Helicopter Wind-Tunnel Model with a 3.15-meter Diameter Single Rotor," NASA TM 80051, Langley Research Center, 1979.
- [30] B. Thwaites, "Approximate Calculation of the Laminar Boundary Layer," *Aeronautical Quarterly*, vol. 1, pp. 245-280, 1949.
- [31] N. Curle, "A Two-Parameter Method for Calculating the Two-Dimensional Incompressible Laminar Boundary Layer," *The Journal of the Royal Aeronautical Society*, vol. 71, pp. 117-123, 1967.
- [32] J. F. Nash and J. G. Hicks, "An Integral Method Including the Effect of Upstream History on the Turbulent Shear Stress," in *Computation of turbulent boundary layers - 1968 AFOSR-IFP-Stanford Conference*, Stanford, 1969.
- [33] N. W. Schaeffler, B. G. Allan, C. Lienard and A. L. Pape, "Progress towards fuselage drag reduction via active flow control: A combined CFD and experimental effort," in *36th European Rotorcraft Forum*, Paris, 2010.
- [34] K. Pahlke, "The GOAHEAD Project," in *33rd European Rotorcraft Forum*, Kazan, Russia, 2007.
- [35] B. Benoit, A.-M. Dequin, K. Kampa, W. von Grünhagen, P.-M. Basset and B. Gimonet, "HOST, a General Helicopter Simulation Tool for Germany and France," in *American Helicopter Society 56th Annual Forum*, Virginia Beach, Virginia, USA, 2000.
- [36] J.-H. Wendisch and J. Raddatz, "Validation of an unstructured CFD solver for complete helicopter configurations with loose CSD-trim coupling," in *40th European Rotorcraft Forum 2014*, Southampton, England, 2014.
- [37] M. Biava, W. Khier and L. Vigevano, "CFD prediction of air flow past a full helicopter configuration," *Aerospace Science and Technology*, vol. 19, no. 1, pp. 3-18, 2011.
- [38] D. M. Somers, "Design and Experimental Results for a Natural-Laminar-Flow Airfoil for General Aviation Applications," 1981.